The Seismic Record
A journal of the Seismological Society of America

The 1886 Charleston, South Carolina, Earthquake: Relic Railroad Offset Reveals Rupture

Roger Bilham[1] and Susan E. Hough*[2]

Abstract

In the absence of documented surface rupture during the 1 September 1886 Charleston earthquake, there has been considerable speculation about the location and mechanism of the causative fault. We use an inferred coseismic offset of the South Carolina Railroad and additional numerical constraints to develop an elastic deformation model—a west-dipping fault following strands of two previously identified faults. The constraints are consistent with a blind rupture with 6.5 ± 0.3 m of dextral slip and 2 ± 0.5 m of reverse slip below 450 m depth. We propose that repeated slip on this fault has raised the Penholoway Marine Terrace >6 m since ~770 ka. The inferred coseismic slip on the fault in an M_w 7.3 earthquake is consistent with the distribution of damage in 1886.

Cite this article as Bilham, R. and S. E. Hough (2023). The 1886 Charleston, South Carolina, Earthquake: Relic Railroad Offset Reveals Rupture, *The Seismic Record*. **3**(**4**), 278–288, doi: 10.1785/0320230022.

Introduction

The 1 September 1886 Charleston, South Carolina, earthquake (9:50 p.m. local time on 31 August 1886) caused chandeliers to swing in Detroit and Cuba, and was felt over much of the eastern United States (Dutton, 1890; henceforth, D1890; Fig. 1a). The earthquake predates the instrumental era, but an intensity-based magnitude of 6.6–7.3 has been estimated (Johnston, 1996; Bakun and Hopper, 2004). The earthquake occurred in an intraplate region with no readily identifiable surface faults, and there remains no consensus regarding the fault that slipped in 1886 despite considerable investigative effort (Behrendt *et al.*, 1981; Hamilton *et al.*, 1983; Rhea, 1989; Durá-Gómez and Talwani, 2011; Chapman *et al.*, 2016; Marple and Hurd, 2022; Pratt *et al.*, 2022). To develop a rupture model, we identify constraints of potential utility to constrain the geometry of faulting in 1886. We then use these constraints to develop a first-order elastic deformation model.

Initial identified constraints based on prior work include the following: (1) stratigraphic evidence (Weems *et al.*, 2014) for uplift or tilt of the Penholoway Marine Terrace (Rhea, 1989; Fig. 1); (2) fault offsets identified in seismic reflection profiles (Pratt *et al.*, 2022); (3) historical maps indicating ~1 m of uplift at Summerville between 1884 (Gannett, 1884) and 1919 (see Data and Resources); (4) archaeological evidence indicating a lack of uplift at Fort Dorchester (Ruddy and Howard, 2017; Fig. 1); and (5) west-dipping seismicity (Chapman *et al.*, 2016) below the Penholoway Terrace, which may illuminate active faulting. These indications of faulting are all north of 32.9°. We omit a purported dextral offset apparent in a photograph of the Charleston-Savannah Railroad west of Rantowles taken days after the earthquake (D1890), which quantitative optical evaluation shows could have been associated with lateral spreading.

The first listed constraint draws from published results (Weems *et al.*, 2014), but the implications of stratigraphic data have not been considered previously. The highest points of the Penholoway Terrace, at 27–29 m above sea level, are mantled with ~770 ka Pleistocene shoreline berms. These relatively recent sediments are unexpected here, because shorelines with similar elevations 40 km to the west have been dated at 1.2 Ma (Weems *et al.*, 2014). Deposits of similar age to those on the

1. CIRES, University of Colorado, Boulder, Colorado, U.S.A., https://orcid.org/0000-0002-5547-4102 (RB); 2. U.S. Geological Survey, Pasadena, California, U.S.A., https://orcid.org/0000-0002-5980-2986 (SEH)

*Corresponding author: hough@usgs.gov

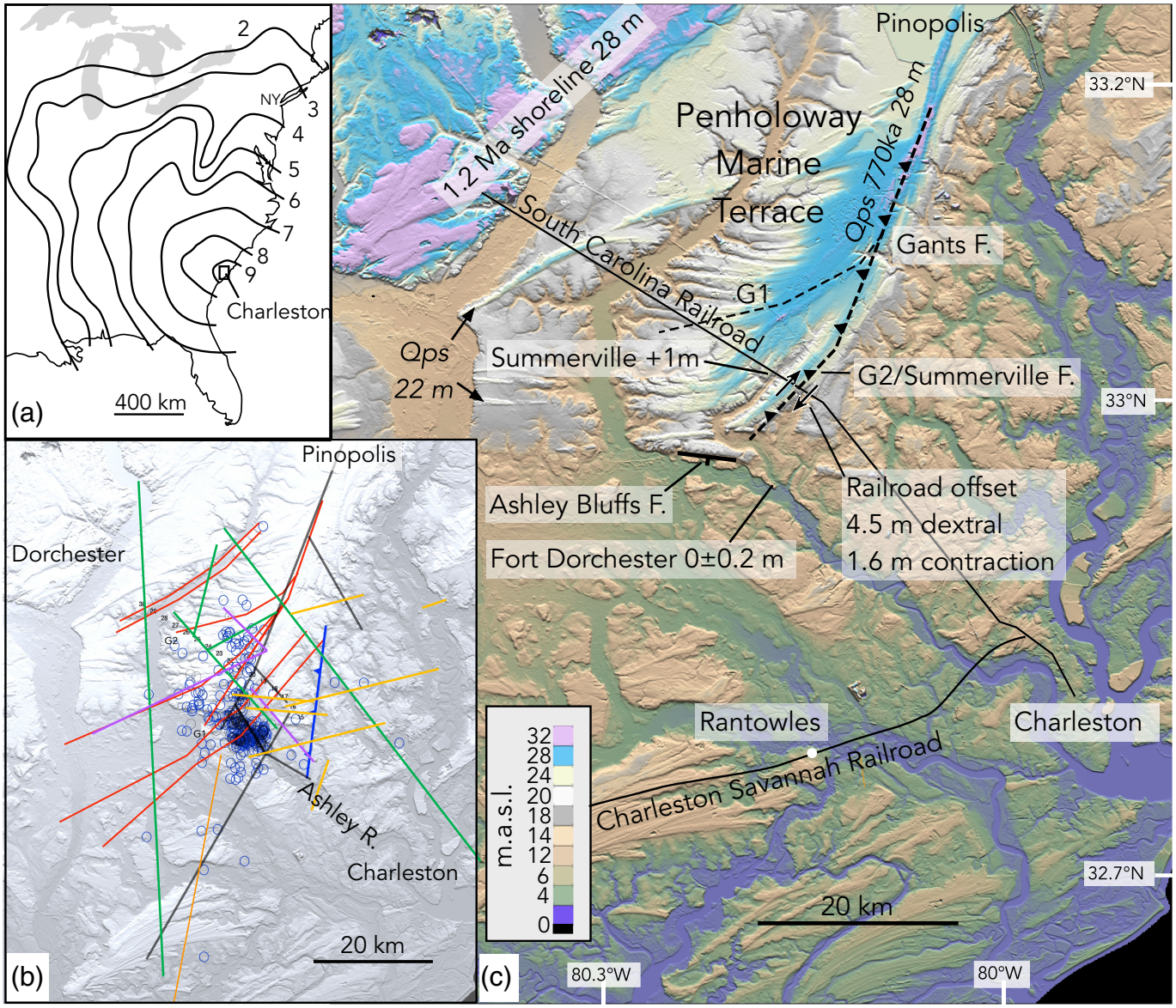

Figure 1. (a) Location map with Rossi–Forrel intensity contours (Dutton, 1890). (b) Faults proposed by the previous authors (colored lines) with 1977–2005 relocated seismicity (blue circles; Chapman *et al.*, 2016). (c) Morphology of the Charleston region with locations of key coseismic contraints and faults discussed in text (the same area as panel b), including 1-m elevation change in Summerville and ±0.2 m bound on elevation change at Fort Dorchester. The Penholoway Terrace is mantled by younger sediments (*Qps*) than nearby locations at similar elevations (Weems *et al.*, 2014), supporting the interpretation proposed by Rhea (1989) that this terrace has been uplifted or tilted by slip in repeated earthquakes.

Penholoway Terrace west of Summerville are found at lower elevations (19–22 m), 20 km west of Summerville (Fig. 1c), and suggest an interpretation that the Penholoway Terrace has risen ≥6 m relative to these deposits in the past 770 ka. Tectonic control of the elevated region was first proposed by Rhea (1989). Pleistocene and recent tectonic uplift and tilting of the Penholoway Terrace are consistent with doming inferred from concave-down river profiles that have incised its southern scarp and flanked its western edges (Rhea, 1989).

In November 2022, we undertook fieldwork with the objective of determining the precise locations of railroad mile markers described in archival reports (D1890). During these investigations, we identified the previously unrecognized dextral offset of the South Carolina Railroad (SCRR; now the Norfolk Southern line) southeast of Summerville (Fig. 2). We mapped the track along this segment using

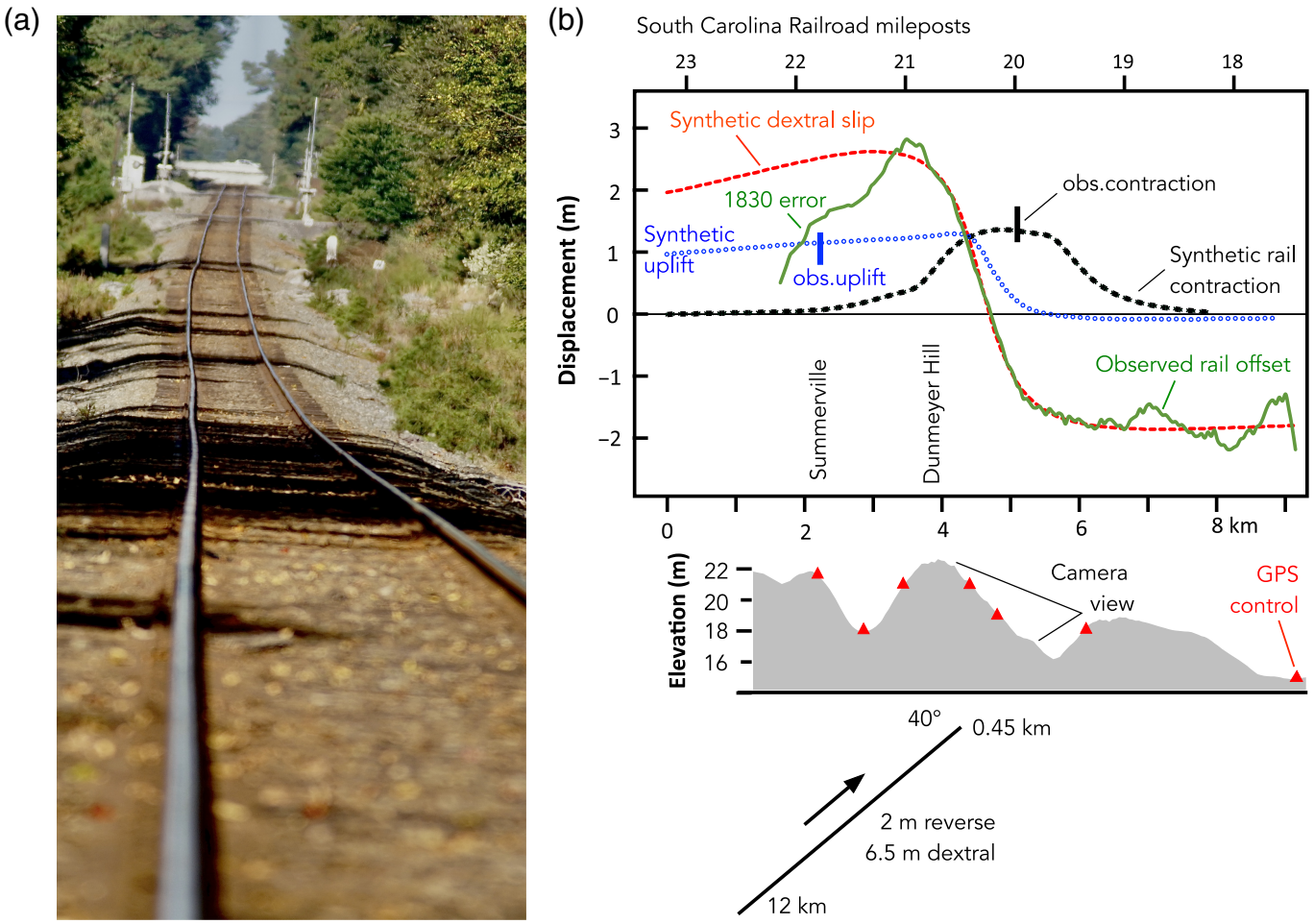

space-based imagery. We estimated the accuracy of these measurements to be ±5 cm by spot-checking with sparse global positioning measurements. The inferred 4.5 ± 0.3 m offset (Fig. 2) is close to the mapped location of the down-to-east Summerville fault (Fig. 1c; Weems *et al.*, 2014). To the northwest of SCRR milepost 21, the railroad track veers N0.7°W from the arctan geometry anticipated from a buried dextral fault—a misalignment that can be attributed to the initial survey of the railroad in which it crested Dunmeyer Hill, obscuring line-of-sight viewing of the tracks and necessitating the establishment of an instrumentally derived heading (Fig. 2). With this caveat, the 4.5 ± 0.3 m dextral offset is a notable geometrical kink in the railroad (Fig. 2). Our identification of this offset as coseismic is supported by a contemporary observation indicating that the rail bed was "forced to Right" (Peters and Herrmann, 1986, p. 55). Unlike other documented railroad offsets in low-lying swampy regions (D1890), this offset is confined between railroad cuttings.

Figure 2. (a) November 2022 photo of railroad tracks offset by one track width as they ascend the southeast flank of Dunmeyer Hill (photograph: Roger Bilham). (b) Synthetic deformation for planar dislocation with geometry and parameters shown compared to observed data. Contraction is depicted in m/km with a 2-km averaging window. Camera view indicated. GPS, Global Positioning System.

Tests of Previous Proposed Fault Geometries

Several previous studies of the region have suggested causative fault(s) for the mainshock. We now explore models based on these suggestions. The published rupture scenarios discussed in the following paragraphs did not include assigned slip or a slip distribution. We therefore assign uniform planar slip to proposed ruptures, with a numerical value consistent with a cumulative moment magnitude, M_w, 7.0–7.3. We next calculate the surface uplift arising from this uniform slip and compare it with the vertical constraints discussed earlier: that Summerville was approximately 1 m higher after the earthquake than before and

that the wharves at Fort Dorchester have remained at their present level since the seventeenth century. We also calculate the Coulomb stress changes associated with modeled faults (Toda *et al.*, 2005), although we observe that their relationship to present-day seismicity may not be diagnostic for an earthquake over 100 yr ago.

We first consider the causative faults proposed by Durá-Gómez and Talwani (2011) (Fig. 3b,c). We assign an oblique slip of 3.2 m to each half of the Woodstock fault and a 2 m reverse slip to faults in the intervening jog. Despite Coulomb changes calculated for this slip geometry being approximately coincident with present-day seismicity (Fig. 3c), the 1 m uplift contour arising from this slip distribution (Fig. 3b) passes both through Summerville and through Fort Dorchester. Hence, this fault geometry cannot be considered viable for the 1886 rupture.

We also consider the restraining bend model proposed by Marple and Hurd (2022) (Fig. 3d–f). In one scenario, slip on an inferred vertical dextral fault, ML4, results in stress that induces slip on the ≈N80°E Deer Park Lineament (DPL; Fig. 3d). We assigned 5 m of slip to ML4 and calculated the Coulomb failure stress imposed on DPL in a depth range of 1–10 km. Although the Coulomb change has the correct polarity, the location of DPL is not optimum for induced slip. We then assigned 4 m of dextral slip to DPL and 5 m to ML5. A range of slips (and magnitudes) can be assigned to ML4 without impacting the effect of elevation changes at the western end of the DPL, which the authors propose to be the causative fault for the 1886 mainshock. This model is untenable because coseismic uplift near the western end of the DPL is opposite to that observed (Fig. 3e). The cumulative Coulomb stress change arising from slip, moreover, peaks to the west of present-day seismicity (Fig. 3f).

In Figure 3g–i, we show the consequences of slip on the 43° W reverse fault proposed by Chapman *et al.* (2016). The fault is based on an inferred rupture from 6.5 to 14 km depth with a top edge between 80.174° W, 33.084° N, and 80.215° W, 32.744° N (Chapman, Virginia Tech, written comm., 2023). This fault with 38 km of length and ∼3 m of slip (M_w 7.0) results in 40 cm of uplift at Fort Dorchester (Fig. 3g), which is both inconsistent with the absence of observed uplift at this location and with the absence of ponding of the Ashley River in 1886 (D1890). Doubling the mean slip raises M_w to 7.3, but if only the northern one-fourth of this fault slips, either as a reverse fault or with oblique slip >5 m (Fig. 3h), it results in 1 m of uplift at Summerville with zero uplift of Fort Dorchester, consistent with constraints. In this modified scenario, the resulting Coulomb stress changes are also consistent with the triggered seismicity currently observed (Fig. 3i). The modified model, however, neither matches the geometry of the Penholoway Terrace nor is it consistent with the observed dextral offset (Fig. 2).

None of the previously proposed models satisfactorily predicted zero uplift at Fort Dorchester. Minor adjustments to fault slip and fault location can be contrived to suppress the amount of uplift at this location, but uplift is an unavoidable consequence of significant slip if the fault model remains guided by the present-day distribution of seismicity.

A Rupture Model for the 1886 Earthquake

The newly identified SCRR railroad offset at the mapped location of the Summerville fault provides a key constraint for the development of an elastic deformation model. The Summerville fault approximately coincides with the G2-Gants fault identified from seismic reflection lines (Pratt *et al.*, 2022). We refer to these fault strands collectively as the G2-Summerville fault (Fig. 1c). The 1.5 km width of the zone of dextral offset (Fig. 2b) centered on the G2-Summerville fault requires that coseismic slip (and any subsequent afterslip) be no shallower than 450 m. Current microseismicity to the west of the fault suggests that the G2-Summerville fault may dip to the west at 40°–45° (Chapman *et al.*, 2016). Calculations for dislocations with this range of dips in an elastic half-space show that subsurface dextral slip of 6 ± 0.5 m is needed to match the 4.5 ± 0.5 m of observed dextral surface offset here. This increased subsurface slip arises in part from its proximity to the southern end of the inferred fault.

For along-strike constraints for rupture, we invoke geological and macroseismic observations. The geomorphic southernmost expression of the G2-Summerville fault terminates at 32.98° N. The northern limit of faulting is unconstrained by direct observation. However, a report listing economic relief payments made by an Earthquake Relief Committee (Simons, 1887) includes a single modest payment for damage in Pinopolis. In contrast, the report indicates that, of $51,000 in immediate relief payments, over $20,000 was paid for damage in Summerville. Like Summerville, Pinopolis was established in the early nineteenth century as a retreat from summer heat in low-lying areas closer to Charleston (Walsh and Guerry, 2006). Photos of historical structures reveal similar construction as Summerville (Walsh and Guerry, 2006). Available data thus suggest that damage at Pinopolis in the earthquake was less severe than at Summerville.

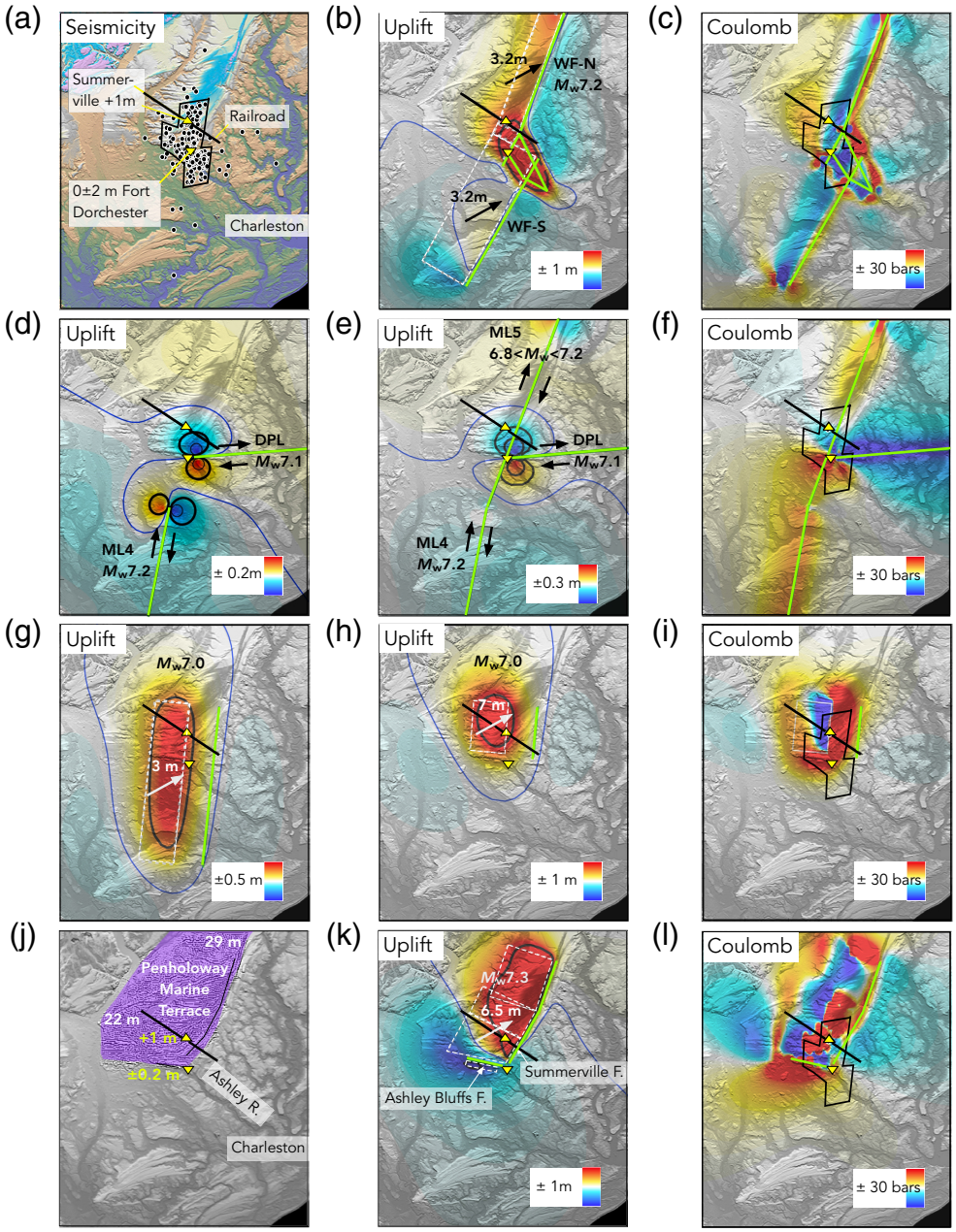

Figure 3. (a) Recent seismicity (Chapman *et al.*, 2016), inferred 1-m uplift at Summerville (yellow triangle), and inferred ~zero uplift at Fort Dorchester (inverted yellow triangle). Panels (b–i) present predicted deformation and Coulomb stress change for models developed from previously proposed rupture scenarios: (b,c) antidilational fault jog between north and south segments of the west-dipping dextral Woodstock fault (Durá-Gómez and Talwani, 2011); (d–f) restraining bend between two vertical dextral faults (Marple and Hurd, 2022); (g–i) 43° west-dipping reverse fault with ≈3 m of slip (Chapman *et al.*, 2016), including longer and shorter assumed rupture lengths (panels g and h, respectively). Panels (j–l) present a preferred model (this study), including (j) an outline of Penholoway Terrace with proposed faults with elevations of ~770 ka shoreline berm (Weems *et al.*, 2014). In panels showing uplift (panels b,d,e,g,h,k), red and blue indicate uplift and subsidence, respectively; a thin blue contour indicates smoothed zero uplift; and black contours outline discretized vertical deformation. Dashed white polygons outline a map view of modeled rupture planes, with slip and corresponding M_w indicated. The black line indicates the South Carolina railroad between mileposts 17 and 30. In panels showing predicted Coulomb stress change (panels c,f,i,l), stress is calculated at 3–6 km depth; red indicates enhanced stress on west-dipping thrust planes. Coulomb stress change for geometries in panels (d) and (g) is not shown. The polygon enveloping 95% of the recent microseismicity in panel (a) is compared with predicted Coulomb stress change (panels c,f,i,l).

Accordingly, we terminate the northward rupture at latitude 33.2° N (Fig. 1c), yielding a rupture length of 27 km.

Contemporary field observations also describe buckling of the SCRR near the offset shown in Figure 2 (D1890, p. 285). A diagram of a 15-m long segment of buckled rail from this location (D1890) indicates 1.6 m of along-line shortening with 18 cm of dextral offset. We use this buckled rail as an approximate measure of convergence across the fault. A reverse slip of 2 m provides reasonable agreement with both ≈1 m of uplift at Summerville and with rail convergence near milepost 20 (Fig. 2b). The documented buckling provides a weak constraint on the locus of uplift. More notably, the coincidence of the G2-Summerville fault with Dunmeyer Hill supports the interpretation that the fault (and 1886 earthquake) accommodates both dextral and reverse motion. When modeled as slip in an elastic half-space, the assumed rupture results in uplift contours that approximate the geometry of the Penholoway Terrace (Doar and Kendall, 2014). Based on the inferred relationship between long-term uplift of the Penholoway Terrace and uplift in 1886 evident in our initial model with uniform slip, we adjusted both the width and slip in segments of the G2-Summerville fault in iterative forward models to more closely emulate the geometry of the elevation contours of the terrace. To improve the fit to the morphology west of Summerville, for example, it was necessary to extend the southernmost segment of the fault in the subsurface from a rectangle normal to strike to a trapezoid abutting the South Summerville Scarp, increasing the rupture length by 10% to ∼30 km (Table 1). The slip vectors so derived lie close to N60°E; the azimuth of SH_{max} is determined from focal mechanisms and borehole breakouts (Lundstern and Zoback, 2020). Surface uplift from this rupture does not extend to the eastern edge of the Penholoway Terrace. For this to occur, a secondary eastward splay with a shallower dip must be invoked, rooting in the main rupture at depth (e.g., Fagereng *et al.*, 2019). The synthetic uplift of the Penholoway Terrace associated with the main rupture tilts gently to the west, consistent with parallel drainages developed on its western flank and with short immature drainages along its eastern scarp, as would be expected from a blind thrust dipping to the west.

Our preferred rupture model includes minor moment release on a tear fault along the southern edge of the Penholoway Terrace, which we call the Ashley Bluffs fault (Fig. 1), following lineations along the southern edge of the terrace. The proposed Ashley Bluffs fault lies in a quadrant of extensional strain in which normal faulting would be anticipated from slip in the dextral mainshock. Our model includes relatively minor (∼1 m) surface slip on this fault. Several lineations are evident north and west of the Ashley Bluffs fault that are consistent with normal faulting within a fishtail splay at the southwest end of the proposed G2-Summerville rupture (Weems *et al.*, 2014). The relationship of these inferred minor faults to mainshock slip on the G2-Summerville fault in 1886 may be similar to faulting observed in the 1897 Shillong Plateau earthquake (England and Bilham, 2015). In 1897, subsurface reverse faulting on the Oldham fault below 7 km tightened and raised a surface anticline >10 m, whose surface expression was truncated to the west by surface rupture of up to 11 m on the ≈20 km long Chedrang normal fault.

To the southeast of the G2-Summerville and proposed Ashley Bluffs faults, a zone of disruption in the subsurface has been interpreted as faulting and folding down to the south (Chapman *et al.*, 2016). Present-day seismicity near here dips 43° W and suggests that this region may continue to respond to stress induced by the 1886 earthquake and/or ongoing secular strain, but because neither significant uplift in the hanging wall nor significant subsidence in the footwall is recorded in the morphology or postcolonial history of docks and moorings near Charleston (Ruddy and Howard, 2017), we consider its cumulative historical slip and potential for future seismic risk to be small.

Our preferred parameters for mainshock slip (Table 1) imply a moment magnitude for the earthquake of M_w 7.3. This estimate reduces to 7.2 if 1886 coseismic slip extends no deeper than 8 km on a 45° dipping fault or if we have overestimated the length and/or slip of rupture to the north. We explored synthetic models further by examining the consequences of introducing minor slip on the Ashley Bluffs fault and the G1 fault of Pratt *et al.* (2022) (Table 1), assuming this latter fault also slips in a reverse sense at 40°–45°. G1 slip of ≤1 m down to the south does not substantially alter the area of the 1 m uplift contour and raises the cumulative magnitude by less than 0.05 M_w units. A slip of <1 m on the Ashley Bluffs fault is consistent with a lack of uplift of the historical docks at Fort Dorchester (Ruddy and Howard, 2017). At least two prominent aftershocks were documented within hours of the mainshock (D1890). In the scenarios discussed here, these may have occurred as $M_w \sim 6$ earthquakes on the G2-Summerville fault, the Ashley Bluffs fault, or a hypothesized shallow splay fault; but it is possible that the reported aftershocks occurred on faults elsewhere in the region.

Table 1
Synthetic Fault Segment Parameters Selected to Emulate Penholoway Marine Terrace Uplift and Railroad Deformation

Name	Start (° W)	Start (° N)	End (° W)	End (° N)	*L* (km)	Dextral (m)	Dip-Slip (m)*	Dip (°)	Top (km)	Base (km)
Ashley Bluffs obs	80.2270	32.968	80.119	32.964	2.6	0	1	79° S	0.1	5
Ashley Bluffs adj	80.2774	32.977	80.119	32.964	7.4	0	1	79° S	0.1	5
G2-SummervilleN	**80.057**	**33.190**	**80.102**	**33.080**	**13**	**2.5**	**–2**	**40° W**	**0.6**	**10**
G2-SummervilleC	**80.102**	**33.080**	**80.135**	**33.024**	**7**	**4.8**	**–2**	**40° W**	**0.5**	**12**
G2-SummervilleS	**80.135**	**33.024**	**80.177**	**32.985**	**6**	**6.5**	**–2**	**40° W**	**0.45**	**12**
G2-SummervilleΔ	**80.333**	**32.964**	**80.235**	**32.964**	**2–4**	**6.3**	**–2**	**40° W**	**0.5**	**12**
G1 Gants fault	80.1141	33.067	80.212	32.937	3.1	0	1	40° NW	0.2	2
G1 Gants fault	80.0892	33.109	80.1092	33.086	5.1	0	1	40° NW	0.2	4
G1 Gants fault	80.1092	33.086	80.1566	33.062	8.8	0	1	40° NW	0.2	8

Bold segments yield cumulative mainshock moment magnitude M_w 7.3. Mapped (obs) and adjusted (adj) lengths for slip on the Ashley Bluffs fault are indicated in the first two rows. Segment indicated Δ provides the southern bound to a triangular segment to the west of the southernmost G2-Summerville fault. Fault segment endpoints for the previously proposed faults (Pratt *et al.*, 2022) were estimated from published maps.
*Negative values represent reverse slip.

Our proposed elastic deformation model is a simplified representation of rupture and not unique, but it satisfies all the identified constraints. The 4.5 m permanent offset to the railroad southeast of Summerville is crucial to quantifying dextral slip in the earthquake. The wavelength of this offset determines its closest approach to the surface (450 m), and contemporary descriptions of railroad shortening (1.6 m) determine approximate reverse slip (2 m). The resulting elastic model forecasts 1 m of uplift at Summerville with zero uplift at Fort Dorchester, consistent with observations. The region of uplift approximates the surface contours of the Penholoway Marine Terrace (Figs. 3j,k and 4), leading us to deduce that, as originally proposed by Rhea (1989), multiple earthquakes may be responsible for its current elevation. Although the recent background seismicity may or may not have been controlled by an earthquake over 100 yr ago, the Coulomb change resulting from slip in the model at 3–6 km depths (Fig. 3l) is consistent with the location of present-day seismicity documented by Chapman *et al.* (2016).

Coseismic Slip and Shaking Intensity in 1886

Our preferred M_w 7.3 magnitude is consistent with the large $\sim 5 \times 10^6$ km^2 felt area of the rupture. This M_w is at the upper end of both the range of the previously estimated magnitudes (Johnston, 1996; Bakun and Hopper, 2004) and the range of fault slips for a fault with a length ≤30 km (Thingbaijam *et al.*, 2017). Relatively large slip is, however, in line with high stress drops observed generally for mid-continent earthquakes (Scholz *et al.*, 1986).

We now briefly examine the anticipated intensity of shaking calculated for the earthquake with that documented in the epicentral region. We use 17 available ground-motion models (GMMs) (Goulet *et al.*, 2021) to calculate peak ground acceleration (PGA) and peak ground velocity (PGV) for M_w 7.25, using a linear average of values for M_w 7.0 and 7.5 (Goulet *et al.*, 2021). The GMMs are based on R_{rup}—the nearest distance to the rupture. We then use the combined PGA and PGV ground-motion intensity conversion equation (Worden *et al.*, 2012) to estimate the predicted modified Mercalli intensity (MMI). The models are developed for a reference hard-rock site condition with a time-averaged shear-wave velocity of 3000 m/s (Goulet *et al.*, 2021). We do not include site response terms because of the expected complexity of strong-motion site response (Ambraseys and Sarma, 1969; Borcherdt, 1970; Beresnev *et al.*, 1995). Contemporary reports document, for example, that damage was worse in parts of Charleston underlain by artificial fill (D1890), but extant photographs (see Data and Resources) suggest limited structural damage to structures adjacent to large sand blows, consistent with nonlinear deamplification of high-frequency shaking (e.g., Rajaure *et al.*, 2017). Ground motions will be explored in more detail in subsequent work.

Our modeling predicts MMI 8–9.4 shaking within ~10 km of the rupture (Fig. 4)—a swath that includes the town of Summerville, where shaking was reportedly more severe than in Charleston (D1890), and Lincolnville, where "violence was apparently a little greater than at Summerville" (D1890, p. 277). Lincolnville (Fig. 4) was the closest settlement to the surface projection of the proposed rupture.

Our modeling predicts MMI (see Data and Resources) 7–9.0 throughout much of the region between Summerville and Charleston (Fig. 4). The near-field intensity distribution is poorly constrained in most locations due to a paucity of structures in the low country. In Ladson, for example, extant reports only state that chimneys collapsed and wooden houses were "severely shaken" at the small railroad station (D1890, p. 286). MMI 9.1 is predicted at this location (Fig. 4). In the city of Charleston, brick and other masonry structures sustained considerable damage (D1890), but only 7% of wood-frame structures sustained damage (Robinson and Talwani, 1983), implying MMI ~8 (see Data and Resources). Predicted MMI 7–9 shaking throughout the low-lying elevations between Charleston and Summerville is consistent with available constraints on near-field shaking, under the expectation that ground motions were amplified in some places by a combination of gross nonlinear site response and, potentially, linear amplification of shaking at longer periods (Ambraseys and Sarma, 1969; Borcherdt, 1970; Fig. 4).

Discussion and Conclusions

We have presented an elastic deformation model for the 1886 Charleston earthquake. Our rupture satisfies the sparse available constraints on coseismic deformation but is nonunique, and we expect it will be refined by future work, including field investigations, active-source studies, and so on. Our preferred rupture model suggests that persistent cumulative slip on the G2-Summerville fault, with slip and geometry similar to that of the 1886 earthquake, may be responsible for the uplift and westward tilt of the Penholoway Terrace by 5–7 m since the mid Pleistocene (≈770 ka), consistent with the interpretation of Rhea (1989). If this scenario is correct, the estimated ratio of dextral to reverse slip (2–2.6) and the inferred cumulative uplift of ≈7 m implies a 12–16 m dextral offset of features on the Penholoway Terrace since its emergence above sea level. If uplift includes its current elevation above its surroundings, the offset may be increased by a factor of two. This is still significantly smaller than the dextral 520 m offset reported for the uppermost beach berm on this terrace (Marple and Hurd, 2022). This offset is, however, uncertain due to the poor definition of the berm and its shallow (~20°) obliquity in which it is inferred to cross the fault.

If the Penholoway Terrace has been raised ≈7 m by earthquakes with similar uplift that occurred in 1886 (≈1 m), the average interval between these earthquakes must be of the order of 100 ka. However, paleoseismic studies in the region (Tuttle *et al.*, 2019) indicate that strong shaking occurs at 500–5000 yr intervals, which implies either that the fault may slip in less severe earthquakes or that other faults in the area are active. Geodetic studies (Trenkamp and Talwani, 2005) reveal anomalously high strain rates to the southwest of the Penholoway Terrace, suggesting renewal intervals of hundreds of years. Present-day seismicity ($1.5 < M_w < 4.5$) occurs to the southeast of the southern termination of our inferred mainshock rupture. The recent seismicity may result from increased coseismic stress in a compressional quadrant of the mainshock (Fig. 2l), but we conclude that significant slip on the west-dipping fault defined by these earthquakes is inconsistent with local surface morphology and thereby may not pose a significant seismic risk. Regions to the northeast and southwest of the rupture were stressed by, or released stress from, the earthquake and merit further study.

Our proposed model for the 1886 rupture yields an M_w estimate of 7.3 on the upper end of the range inferred by the previous studies (Johnston, 1996; Bakun and Hopper, 2004). It is now recognized that intensity-based magnitudes provide only a weak constraint on M_w (Lucas *et al.*, 2023). For hazard applications based on moment magnitude, our modeling of rupture parameters provides a more direct and reliable estimate of M_w. This independent estimate of M_w may be useful to refine intensity-prediction equations for $M_w > 7$ earthquakes in eastern North America, which remain poorly constrained (Goulet *et al.*, 2021). Our elucidation of active faulting in the Charleston seismic zone is also a necessary first step to refine our understanding of seismogenesis in a region that has remained enigmatic.

Data and Resources

The 1 m digital elevation models (DEMs): https://opentopography.org (last accessed April 2023). Historical topo maps for the Charleston region: https://ngmdb.usgs.gov/topoview/viewer/#11/32.9125/-80.0131 (last accessed April 2023). Macroseismic data: Dutton (1890). Intensity scale: https://www.usgs.gov/programs/earthquake-hazards/modified-mercalli-intensity-scale (last accessed June 2023). Historical

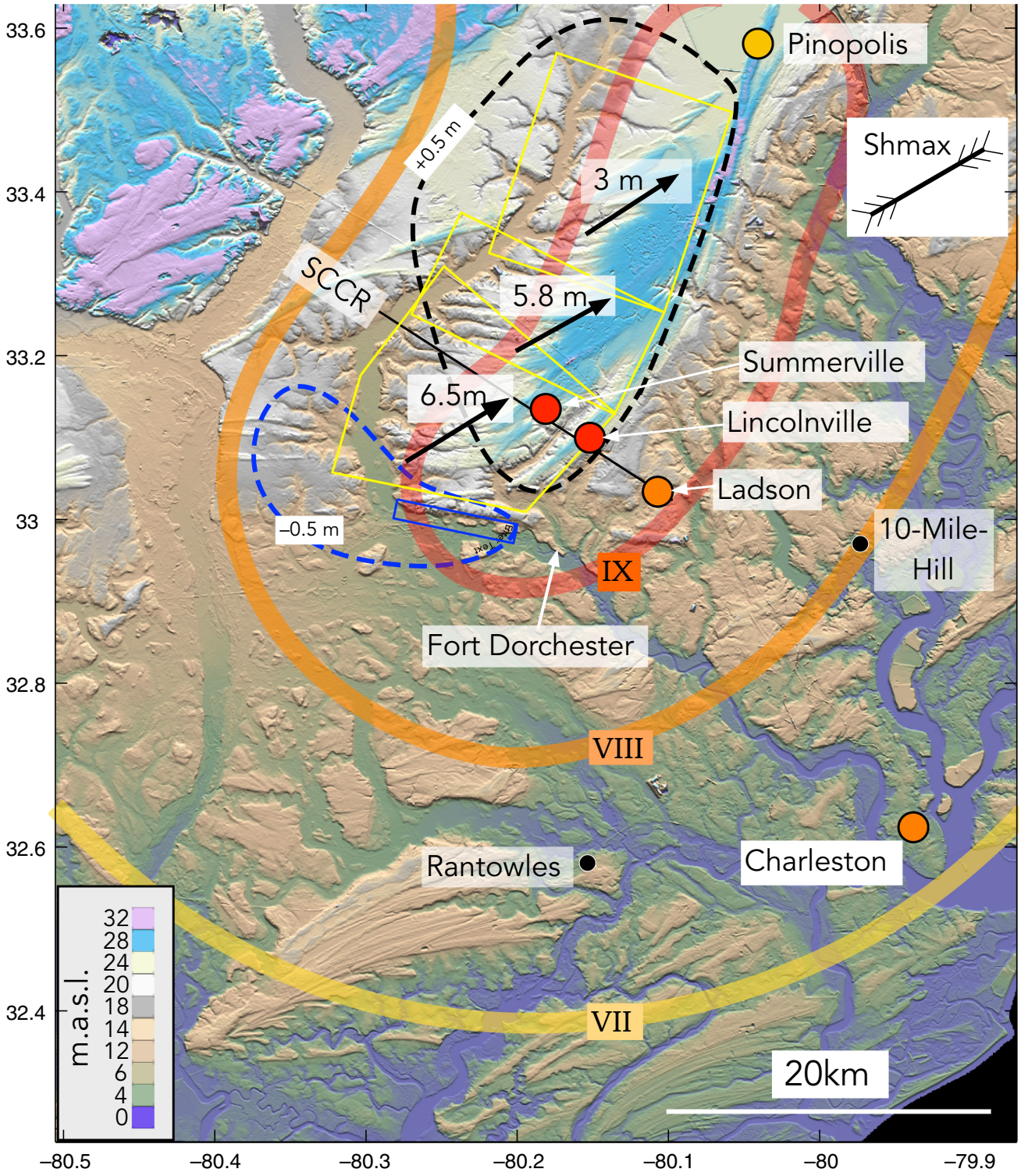

Figure 4. Uplift contours (dashed lines at 50 cm intervals) for the model developed to emulate uplift and dextral slip on the G2-Summerville fault in 1886 (Table 1; M_w 7.3). Yellow polygons indicate simplified west-dipping planar dislocations invoked to emulate curved rupture, with slip vectors indicated. Circles indicate observed shaking intensities at select sites. Synthetic shaking Mercalli intensity contours (VII–IX using the same colors to depict circled intensities) are derived from rupture parameters using available ground-motion models and ground-motion intensity conversion equations (Worden *et al.*, 2012; Goulet *et al.*, 2021). Topographic shading as in Figure 1.

photograph: https://www.eas.slu.edu/eqc/eqc_photos/1886EQ/wjmjpgs/wjm_h4.html (last accessed June 2023). Three-dimensional elastic models were developed using Coulomb 3.3 (Toda *et al.*, 2005) https://www.usgs.gov/node/279387 (last accessed March 2023).

Declaration of Competing Interests

The authors acknowledge that there are no conflicts of interest recorded.

Acknowledgments

The authors thank T. Pratt for supporting our fieldwork and Earthscope for the loan of equipment, A. Shah and W. Doar for helpful discussions, and Martin Chapman for providing unpublished numerical values for his inferred rupture model. The authors thank Fred Pollitz, Brendan Crowell, Shane Detweiller, Suzanne Hecker, and an anonymous reviewer for constructive feedback. Any use of trade, firm, or product names is for descriptive purposes only and does not imply endorsement by the U.S. Government.

References

Ambraseys, N., and S. Sarma (1969). Liquefaction of soils induced by earthquakes, *Bull. Seismol. Soc. Am.* **59,** no. 2, 651–664.

Bakun, W. H., and M. G. Hopper (2004). Magnitudes and locations of the 1811-1812 New Madrid, Missouri, and the 1886 Charleston, South Carolina, earthquakes, *Bull. Seismol. Soc. Am.* **94,** no. 1, 64–75.

Behrendt, J. C., R. M. miltonHa, H. D. Ackermann, and V. J. Henry (1981). Cenozoic faulting in the vicinity of the Charleston, South Carolina, 1886 earthquake, *Geology* **9,** 117–122.

Beresnev, I. A., K.-L. Wen, and Y. T. Yeh (1995). Nonlinear soil amplification: Its corroboration in Taiwan, *Bull. Seismol. Soc. Am.* **85,** no. 2, 496–515, doi: 10.1785/BSSA0850020496.

Borcherdt, R. (1970). Effects of local geology on ground motion near San Francisco Bay, *Bull. Seismol. Soc. Am.* **60,** no. 1, 29–61.

Chapman, M. C., J. N. Beale, A. C. Hardy, and Q. Wu (2016). Modern seismicity and the fault responsible for the 1886 Charleston, South Carolina, earthquake, *Bull. Seismol. Soc. Am.* **106,** no. 2, 364–372.

Doar, W., and C. Kendall (2014). An analysis and comparison of observed Pleistocene South Carolina (USA) shoreline elevations with predicted elevations derived from marine oxygen isotope stages, *Quat. Res.* **82,** no. 1, 164–174, doi: 10.1016/j.yqres.2014.04.005.

Durá-Gómez, I., and P. Talwani (2011). Finding faults in the Charleston area, South Carolina: 2. Complementary data, *Seismol. Res. Lett.* **82,** no. 4, 599–605, doi: 10.1785/gssrl.82.4.599.

Dutton, C. E. (1890) The Charleston earthquake of August 31, 1886, *U.S. Geol. Surv. Ninth Annu. Rept. 1887-1888*, 528 pp.

England, P., and R. Bilham (2015). The Shillong Plateau and the Great 1897 earthquake, *Tectonics* **34,** doi: 10.1002/2015TC003902.

Fagereng, A., H. M. Savage, J. K. Morgan, M. Wang, F. Meneghini, P. M. Barnes, R. Bell, H. Kitajima, D. D. McNamara, D. M. Saffer, *et al.* (2019). Mixed deformation styles observed on a shallow subduction thrust, Hikurangi margin, New Zealand, *Geology* **47,** no. 9, 872–876.

Gannett, H. (1884). *A Dictionary of Altitudes in the United States*, U.S. Geological Survey, 449 pp., Bulletin 5.

Goulet, C. A., Y. Bozorgnia, N. Kuehn, L. Al Atik, R. R. Young, R. W. Graves, and G. M. Atkinson (2021). NGA-East ground-motion characterization model Part 1: Summary of products and model development, *Earthq. Spectra* **37,** 1231–1282.

Hamilton, R. M., J. C. Behrendt, and H. D. Ackermann (1983). Land multichannel seismic-reflection evidence for tectonic features near Charleston, South Carolina, in Studies related to the Charleston, South Carolina, earthquake of 1886: Tectonics and Seismicity, U.S. Geological Survey, Professional Paper 1313T, doi: 10.3133/pp1313.

Johnston, A. C. (1996). Seismic moment assessment of earthquakes in stable continental regions—III. New Madrid 1811-1812, Charleston 1886 and Lisbon 1755, *Geophys. J. Int.* **126,** 314–344.

Lucas, M. C., S. E. Hough, S. Stein, L. Salditch, M. M. Gallahue, J. S. Neely, and N. Abrahamson (2023). Uncertainties in intensity-based earthquake magnitude estimates, *Seism. Res. Lett.*, in press.

Lundstern, J. E., and M. D. Zoback (2020). Multiscale variations of the crustal stress field throughout North America. *Nat. Commun.* **11,** 1951, doi: 10.1038/s41467-020-15841-5.

Marple, R. T., and J. D. Hurd (2022). Further evidence for the East Coast fault system and faults associated with the Summerville restraining bend and their possible relationship to the 1886 Charleston, South Carolina, earthquake, USA, *Atl. Geosci.* **58,** 99–129.

Peters, K. E., and R. B. Herrmann (1986). *First-Hand Observations of the Charleston Earthquake of August 31, 1886, and Other Earthquake Materials*, W. J. McGee, E. Sloan, G. E. Manigault, and S. Newcomb, *et al.*, South Carolina Geological Survey, Columbia, Bull. 41, 116 pp.

Pratt, T. L., A. K. Shah, R. C. Counts, J. W. Horton Jr, and M. C. Chapman (2022). Shallow faulting and folding in the epicentral area of the 1886 Charleston, South Carolina, earthquake, *Bull. Seismol. Soc. Am.* **122,** no. 4, 2097–2123, doi: 10.1785/0120210329.

Rajaure, S., D. Asimaki, E. Thompson, S. E. Hough, P. Ampuero, S. S. Martin, A. Inbal, and M. Dhital (2017). Strong motion observations of the Kathmandu valley response during the M7.8 Gorkha earthquake sequence, *Tectonophysics* **86,** 1533–1539, doi: 10.1016/j.tecto.2016.09.030.

Rhea, S. (1989) Evidence of uplift near Charleston, South Carolina, *Geology* **17,** no. 4, 311–315.

Robinson, A., and P. Talwani (1983). Building damage at Charleston, South Carolina, associated with the 1886 earthquake, *Bull. Seismol. Soc. Am.* **73,** no. 2, 633–652.

Ruddy, D., and S. Howard (2017). The Dorchester Waterfront: An avocational underwater archaeological report, Part of the

Anthropology Commons Publication Info Published in 2017 http://artsandsciences.sc.edu/sciaa/, The South Carolina Institute of Archaeology and Anthropology https://scholarcommons.sc.edu/mrd_pubs/11/ (last accessed October 2023).

Scholz, C. H., C. A. Aviles, and S. G. Wesnousky (1986). Scaling differences between large interplate and intraplate earthquakes, *Bull. Seismol. Soc. Am.* **76,** no. 1, 65–70.

Simons, W. W. (1887). The earthquake, 1886. Exhibits showing receipts and disbursements, and the applications for relief, with the awards and refusals of the Earthquake Relief Committee in over 2,000 cases of house owners and cases of application for losses in personal property, Lucas, Richardson & Co., Steam Printers, Charleston, 94 pp.

Thingbaijam, K. K. S., M. P. Mai, and K. Goda (2017). New empirical earthquake source-scaling laws, *Bull. Seismol. Soc. Am.* **107,** no. 5, 2225–2246, doi: 10.1785/0120170017.

Toda, S., R. S. Stein, K. Richards-Dinger, and S. Bozkurt (2005). Forecasting the evolution of seismicity in southern California: Animations built on earthquake stress transfer, *J. Geophys. Res.* **110,** no. B5, doi: 10.1029/2004JB003415.

Trenkamp, R., and P. Talwani (2005). GPS derived strain and strain zonation near Charleston, *J. Geophys. Res.* **77,** 84–96.

Tuttle, M., R. Hartleb, L. Wolf, and P. Mayne (2019). Paleoliquefaction studies and the evaluation of seismic hazard, *Geosciences* **9,** 311, doi: 10.3390/geosciences9070311.

Walsh, N. S., and C. A. Guerry (2006). *Plantations, Pineland Villages, Pinopolis, and Its People*, Donning Co., Charleston, 192 pp.

Weems, R. E., W. C. Lewis, and E. M. Lemon (2014). Surficial geologic map of the Charleston region, Berkely, Charleston, Colleton, Dorchester and Georgetown Counties, S. Carolina, *U.S. Geol. Surv. Open File Rept. 2013-1030*, doi: 10.3133/ofr20131030.

Worden, C. B., M. Gerstenberger, D. A. Rhoades, and D. J. Wald (2012). Probabilistic relationships between ground-motion parameters and modified Mercalli intensity in California, *Bull. Seismol. Soc. Am.* **102,** no. 1, 204–221, doi: 10.1785/0120110156.

Manuscript received 15 June 2023
Published online 16 October 2023